A Robust Model Predictive Current Control Strategy with Low Complexity for PMSM

Qianghui Xiao[1], Zhongjian Tang[1], Wenting Zhang[1], Zhi Yu[1], and Zhun Cheng[2, *]

Abstract—Model predictive current control (MPCC) suffers from high computational effort, and control performance is affected by parameter mismatch. In this paper, a robust MPCC strategy with low complexity for permanent magnet synchronous motor (PMSM) is proposed, which reduces the computational complexity and improves robustness. First, a low-pass filter is used to obtain the current actual voltage, and the next-cycle voltage vector is obtained by angle compensation. Alternative voltage vectors (AVVs) are selected according to the location of the next-cycle voltage vector to reduce the control system computation. This part does not use motor parameters to avoid the influence of parameter changes. Then, the relationship between the current error and the input voltage and current sampling value is analysed. A low-complexity current prediction error compensation algorithm is designed to compensate the error caused by the mismatch of motor inductance and flux linkage, which enhances the robustness of the system. Finally, the experimental results demonstrate the correctness and effectiveness of the proposed strategy.

1. INTRODUCTION

Permanent magnet synchronous motor (PMSM) is frequently employed in aerospace [1], electric cars [2], servo systems [3], and other sectors because of its excellent durability and efficiency. A number of new control methods have been proposed and used in PMSM control systems, including sliding mode control [4], robust control [5], model predictive control (MPC) [6], etc., as a result of the increasing demands for motor control performance in recent years. MPC has drawn a lot of interest because of its conceptual simplicity, quick dynamic reaction, and aptitude for dealing with diverse and nonlinear constraints.

The most used MPC strategies are model predictive torque control (MPTC) [7] and model predictive current control (MPCC) [8]. MPTC works by using a model of the motor to predict the future values of torque and flux linkage under the action of different voltage vectors, selecting the one that minimizes the cost function. The cost function of MPTC contains two parameters with different units of torque and flux linkage, which need to be set with weighting coefficient to ensure the good control performance of the system. There is no definite general calculation theory for the weight coefficient of flux linkage and torque, and a large number of experiments and simulations are needed to determine the weighting coefficient. For MPCC, the cost function includes d-axis and q-axis currents, which have the same units and thus do not require weighting coefficient.

Normally, MPC has to traverse all voltage vectors, which is computationally costly. Numerous academics have looked into this in order to lessen the computational burden on control systems. In [9], a table of active prediction vector options is given to select alternative voltage vectors (AVVs) by the position of the stator flux and torque offset. [10] summarizes the rules of vector selection for conventional

---

* Corresponding author: Zhun Cheng (120277982@qq.com).
[1] Hunan University of Technology, Zhuzhou 412007, China. [2] Hunan Railway Professional Technology College, Zhuzhou 412001, China.

MPCC and then takes the vector selected in the previous cycle and its two adjacent active vectors, as well as the zero-voltage vector as AVVs, reducing the number of AVVs from 7 to 4. In [11], a direct torque control switching table is used to reduce the number of vectors to be selected, which is simple and has a fast torque response but produces higher torque and flux linkage fluctuations. In [12], a two-layer generalized decision algorithm is introduced, which splits the cost function into a two-layer cascade, where non-optimal branch terms in the first layer are discarded, and optimal branch elements enter the second layer for further optimization, avoiding exhaustive enumeration of all voltage vectors. A reference voltage-based model predictive control (RV-MPC) strategy is used in [13, 14]. The reference voltage vector is obtained according to the deadbeat principle, and the nearest voltage vector is selected as the optimal vector. In addition, the introduction of duty cycle control achieves the adjustment of voltage vector amplitude [14]. Based on [14], the phase of the voltage vector is adjusted using a virtual vector [15]. However, the reference voltage vector obtained in the case of motor parameter mismatch will deviate from the actual reference voltage vector, so the control performance is affected.

Inaccurate measurements may result in the rated parameters on the motor nameplate not matching the actual parameters. Alternatively, the motor parameters may change during operation due to temperature rise, magnetic saturation, and other factors. In [16], the effect of parameter uncertainty on the FCS-MPCC is analysed. The result shows that the parameter mismatch has a small effect on the dynamic performance of the motor but a large effect on the steady-state performance of the motor. To address this problem, many scholars have proposed solutions and improvements. [17] summarizes the research on FCS-robustness, which is divided into three aspects: disturbance estimation and compensation, prediction model improvement, and online parameter identification.

In [18], an incremental model is employed for prediction, eliminating the stator flux linkage from the prediction model and avoiding prediction error due to flux linkage mismatch. A discrete extended observer is used to obtain corrected inductance information that is compensated into the prediction model, eliminating the effect of inductance parameter mismatch. In [19], the conventional stator current prediction model is replaced by an integral sliding mode observer-based hyperlocal model without motor parameters, and an adaptive Luenberger observer is used to eliminate the effect of resistance variations in the flux linkage prediction model, which improves the robustness of the predictive control. An improved model-referenced adaptive system was applied to identify inductance parameters online, suppressing prediction disturbances caused by inductance mismatch [20]. In [21], the true inductance and flux linkage of the motor are obtained by a function of switching state, compensating the parametric errors of the system. [22] combines the high-frequency current injection method to obtain the motor inductance, flux linkage, and resistance values and uses the parameters obtained by discrimination for deadbeat control to obtain a parameter-corrected reference voltage vector. The method of obtaining the real parameters of the motor through parameter identification increases the complexity of the algorithm and reduces the dynamic response of the system as a result of parameter regulation and convergence. A model-free predictive control technique is used in [23] and [24] that just uses the inputs and outputs of the system and does not use any motor parameters, which eliminates the issue of model mismatch and provides high anti-interference performance and resilience. However, the model-free prediction method requires more expensive hardware sampling circuits.

Another approach to enhance the robustness of motor control is to analyse the relationship between the prediction error and the voltage vector, obtain the possible prediction error, and compensate it by feedforward. In [25], the current prediction error generated by each vector is sampled and stored respectively, compensated the next time the vector is used, and the error value is updated. If a vector is not used for a long time, its corresponding error value will no longer be reliable.

In order to solve the above problems, this paper proposes a low-complexity MPCC strategy for improving the robustness of PMSM control. Firstly, the current voltage vector is obtained through a low-pass filter; the next-cycle voltage vector is obtained through angle compensation; and the nearby fundamental voltage vectors are selected as AVVs. Then the relationship between the applied voltage and prediction error is analysed in the case of the variation of the flux linkage and inductance of the PMSM, and the prediction errors are calculated and compensated for all AVVs. The method reduces the number of AVVs and enhances the robustness of the system against parameter mismatches. The effectiveness of the proposed strategy is verified by experimental results.

2. MATHEMATICAL MODEL OF PMSM AND TRADITIONAL RV-MPCC STRATEGY

In this paper, surface-mounted PMSM is used as the object of study, and the magnetic flux linkage, iron saturation, hysteresis loss, and eddy current are assumed to be negligible.

The stator voltage equation of PMSM in the d-q coordinate system is expressed as:

$$\begin{cases} u_d = R_s i_d + L_s \dfrac{\mathrm{d}i_d}{\mathrm{d}t} - \omega_e L_s i_q \\[2mm] u_q = R_s i_q + L_s \dfrac{\mathrm{d}i_q}{\mathrm{d}t} + \omega_e(L_s i_d + \psi_f) \end{cases} \tag{1}$$

where u_d, u_q are the stator voltages of the d-q axis, respectively. i_d, i_q are the stator currents of the d-q axis, respectively. R_s is the stator resistance, L_s the stator inductance, ψ_f the permanent magnet flux linkage, and ω_e the electrical angular velocity.

Using a first-order antecedent Euler to discretise Equation (1), the current prediction model is obtained as:

$$\begin{cases} i_d^p(k+1) = i_d(k) + \dfrac{T_s}{L_s} \left[u_d(k) - R_s i_d + \omega_e(k) L_s i_q(k) \right] \\[2mm] i_q^p(k+1) = i_q(k) + \dfrac{T_s}{L_s} \left[u_q(k) - R_s i_q(k) - \omega_e(k) L_s i_d(k) - \omega_e(k)\psi_f \right] \end{cases} \tag{2}$$

where k is the current sampling time, $k+1$ the next sampling time, and T_s the sampling period. $i_d(k)$ and $i_q(k)$ are the d-q axis current components at the time, respectively. $i_d(k+1)$ and $i_q(k+1)$ are the d-q axis predicted current components at the next sampling time, respectively.

The control principle block diagram of RV-MPCC is shown in Figure 1. The whole control system consists of the speed outer loop and current inner loop, and q-axis current reference i_q^{ref} is obtained by the proportional-integral (PI) controller processing the speed error of the outer loop. The d-axis current reference i_d^{ref} is set to 0. According to the deadbeat principle, let the predicted value of the current at moment $k+1$ be equal to the reference value, i.e., $\mathbf{i}^p(k+1) = \mathbf{i}^{ref}$, and the reference voltage can be calculated as:

$$\begin{cases} u_d^{ref} = R_s i_d(k) + L_s \dfrac{i_d^{ref} - i_d(k)}{T_s} - \omega_e L_s i_q(k) \\[2mm] u_q^{ref} = R_s i_q(k) + L_s \dfrac{i_q^{ref} - i_q(k)}{T_s} + \omega_e(L_s i_d(k) + \psi_f) \end{cases} \tag{3}$$

As shown in Figure 2, the two-level, three-phase inverter can generate six active voltage vectors $(u_1 - u_6)$ and two different zero-voltage vectors (u_0, u_7), which form six sectors in space (I-VI). RV-MPCC determines the sector where $\mathbf{u}^{ref}$ is located and selects the two active voltage vectors and one
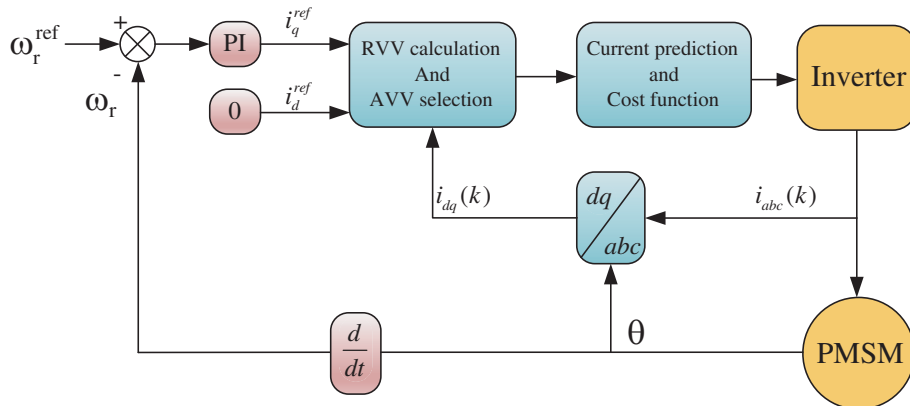

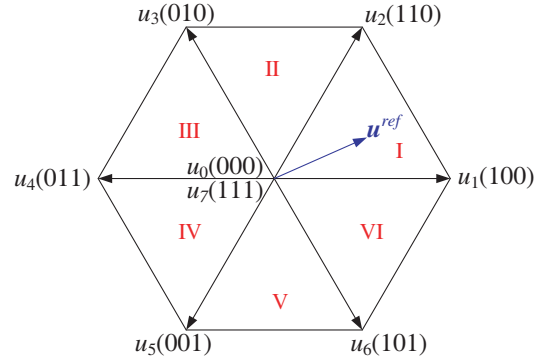**Figure 1.** The control principle block diagram of RV-MPCC.

Figure 2. The voltage vector diagram.

zero-voltage vector adjacent to that sector as AVVs. The number of AVVs is decreased from 7 to 3, reducing the number of predictions. The zero-voltage vectors u_0, u_7 are selected on the basis of the minimum number of switching operations. The current prediction is calculated by Equation (3). The optimal voltage is selected by minimizing the cost function and applied to the motor via the inverter. The cost function g is set to the deviation of the current prediction from the reference value.

$$g = \left(i_d^p(k+1) - i_d^{ref}\right)^2 + \left(i_q^p(k+1) - i_q^{ref}\right)^2 \tag{4}$$

Take Figure 2 as an example. Assuming that the output voltage of the previous cycle is u_1 (100), the reference voltage vector $\mathbf{u}^{ref}$ is located in sector I, so that u_1, u_2, and u_0 (000) are selected as AVVs.

A point worth noting is that in the RV-MPCC strategy, neither Equation (3), which calculates the reference voltage vector, nor Equation (2), which calculates the current prediction, can avoid using the motor parameters. The method is therefore extremely dependent on the motor parameters. If the motor parameters are accurate, and the subtle effects of discretization and switching tube dead zones are ignored, the current at the next sampling moment can be accurately predicted. However, when the actual parameters of the motor do not match the rated parameters, there will be large deviations between the predicted and actual currents, which will have an impact on the system control performance.

3. THE PROPOSED MPCC

3.1. AVVs Selection

The steady-state model of the PMSM is obtained according to Equation (1) as:

$$\begin{cases} u_d = R_s i_d - \omega_e L_s i_q \\ u_q = R_s i_q + \omega_e(L_s i_d + \psi_f) \end{cases} \tag{5}$$

As can be seen from Equation (5), the stator voltage of the motor in steady state is related to the motor parameters, current and speed. The motor current and speed remain constant during steady state. The change in motor parameters is an extremely slow process compared to the short control cycle and can be considered constant. Thus, the actual voltages u_d and u_q are fixed values. The trajectory of the actual voltage vector in the α-β axis system is a circle with respect to the motor parameters, current and speed. Voltage vector trajectory does not change when these parameters do not change. According to this feature, the basic voltage vectors adjacent to the actual voltage vector can be selected as AVVs. The basic voltage vectors which are far away from the actual voltage vector are removed, and the control system calculation is reduced.

A low-pass filter is used to filter out the high frequency switching signals from the historical output voltage to obtain the actual current voltage of the motor. The low-pass filter $Q(s)$ is designed as:

$$Q(s) = \frac{1}{1 + \tau s} \tag{6}$$

where τ is the time constant and is the reciprocal of the cut-off frequency. Cut-off frequency is set to 3 times of the voltage frequency at rated speed, so

$$\tau = \frac{60}{3 \times 2\pi pn} \tag{7}$$

where n is the rated speed of the motor, and p is the pole pair number of the motor.

The actual voltage vector $\widehat{\mathbf{u}}(k)$ at moment k can be obtained as:

$$\widehat{\mathbf{u}}(k) = \mathbf{u}(k-1)Q(s) \tag{8}$$

The motor voltage is rotated at the speed of ω_e, and the predicted voltage vector for the next cycle is obtained by the angle compensation method as:

$$\widehat{\mathbf{u}}(k+1) = \widehat{\mathbf{u}}(k)e^{j\omega_e T_s} \tag{9}$$

After acquiring $\widehat{\mathbf{u}}(k+1)$, the AVVs are selected according to its position, and the principles for selecting the AVVs are as follows:

(1) If the output voltage vector of the previous cycle is a zero-voltage vector, the AVVs of this cycle are 6 active voltage vectors and this zero-voltage vector.

(2) If an active vector is selected as the output vector for two consecutive cycles, in the next cycle, it, its two adjacent active voltage vectors, and a zero-voltage vector are used as AVVs. The zero-voltage vectors u_0, u_7 are selected on the basis of the minimum number of switching operations.

(3) In other cases, the two active voltage vectors adjacent to the sector where $\widehat{\mathbf{u}}(k+1)$ is located and a zero-voltage vector are selected as AVVs.

The introduction of the low-pass filter will result in a delay in the actual voltage vector. The role of the actual voltage vector is to provide a basis for AVVs selection. When the actual voltage vector is inside the sector, the selection of AVVs will not be affected by this delay. When the actual voltage vector is on the edge of a sector, the actual voltage may be located in the previous sector due to the filter delay. However, AVVs selection principles (1) and (2) will compensate this delay by selecting the next active voltage vector in the direction of voltage rotation as an AVV. To summarize, the impact of the delay introduced by the filter on the system performance can be greatly avoided.

3.2. Analysis of AVVs Selection

From the principle of AVVs selection, it is clear that this paper reduces the amount of computation by reducing the number of AVVs for the next cycle of the active voltage vector, so the percentage of the active voltage vector being selected determines the efficiency of reducing the amount of computation. In Equation (5), because the values of the Ri_d and Ri_q terms are small compared to the other terms, the actual voltage amplitude at the steady state of the motor is approximately proportional to the speed. When the motor is operated at high speed, the required voltage is high, and the zero-voltage vector is selected less often, so that AVVs are all basic vectors in fewer cases, with a significant reduction in calculation effort. As the motor speed gradually decreases, the period share of the zero-voltage vector increases, and therefore the effect of reducing the number of calculations gradually decreases. The proposed strategy is simulated on the Matlab/Simulink platform, and the average number of AVVs is collected at 2000 cycles each for different speeds in the steady state case. A graph of the average number of AVVs at different speeds is shown in Figure 3. As can be seen from the graph, the average number of AVVs decreases in an approximately linear trend as the speed rises, in line with the analysis.

3.3. Prediction Error Compensation

The variation of motor parameters will result in degraded control performance. Since the influence of resistance mismatch on the control performance is very small [26], the research object of this paper is the case of inductance and flux linkage mismatch.
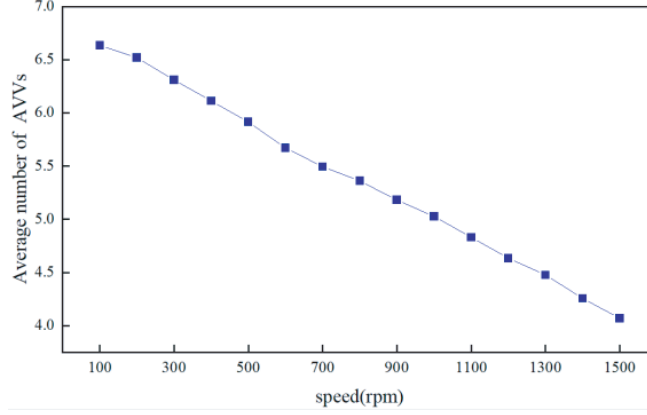
Figure 3. Average number of AVVs at different speeds.

With varying motor inductance and flux linkage, the true current is shown as:

$$\begin{cases} i_d^s(k+1) = i_d(k) + \dfrac{T_s}{L_s + \Delta L}\left[u_d(k) - R_s i_d + \omega_e(k)(L_s + \Delta L)i_q(k)\right] \\ i_q^s(k+1) = i_q(k) + \dfrac{T_s}{L_s + \Delta L}\left[u_q(k) - R_s i_q(k) - \omega_e(k)(L_s + \Delta L)i_d(k) - \omega_e(k)(\psi_f + \Delta\psi)\right] \end{cases} \tag{10}$$

where $i_d^s(k+1)$ and $i_q^s(k+1)$ are the true currents of the d-q axis at moment $k+1$, respectively. ΔL is the change in the true inductance relative to the rated inductance, and $\Delta\psi$ is the change in the true flux linkage relative to the rated flux linkage.

The current prediction error due to inductance and flux linkage mismatch can be obtained by subtracting Equation (2) from Equation (10) as:

$$\begin{cases} erri_d(k+1) = i_d^s(k+1) - i_d^p(k+1) = A(u_d(k) - R_s i_d(k)) \\ erri_q(k+1) = i_q^s(k+1) - i_q^p(k+1) = A(u_q(k) - R_s i_q(k)) + B \\ A = -\dfrac{T_s\Delta L}{L(L + \Delta L)} \\ B = \dfrac{\omega_e T_s(L\Delta\psi - \psi_f\Delta L)}{L(L + \Delta L)} \end{cases} \tag{11}$$

where $erri_d(k+1)$, $erri_q(k+1)$ are the current prediction errors at moment $k+1$.

Because the control period is very short, ω_e, ΔL, and $\Delta\psi$ can be considered constant over several consecutive cycles, so that A and B are constant over several consecutive cycles. From Equation (11), the current prediction errors are related to the applied voltage as well as the current at the present moment. A and B can be calculated from the voltage applied during $k-1$ cycles and the current error measured at moment k.

$$A = \frac{i_d(k) - i_d^p(k)}{u_d(k-1) - R_s i_d(k-1)} \tag{12}$$

$$B = i_q(k) - i_q^p(k) - A(u_q(k-1) - R_s i_q(k-1)) \tag{13}$$

The compensated prediction model is shown as:

$$\begin{cases} i_d^{px}(k+1) = i_d^p(k+1) + A(u_d(k) - R_s i_d) \\ i_q^{px}(k+1) = i_q^p(k+1) + A(u_q(k) - R_s i_q) + B \end{cases} \tag{14}$$

where $i_d^{px}(k+1)$ and $i_q^{px}(k+1)$ are the predicted currents after compensation.

The cost function is set as:

$$g' = \left(i_d^{ref} - i_d^{px}(k+1)\right)^2 + \left(i_q^{ref} - i_q^{px}(k+1)\right)^2 \tag{15}$$

It is worth noting that there is a division calculation in Equation (12), so when the denominator is close to zero, a calculation error occurs, which affects the control performance. In this paper, an optimization mechanism is adopted to avoid this computational error. A threshold value λ is defined. When $|u_d(k-1) - R_s i_d(k-1)| < \lambda$, no update is made to A and B, and the compensation calculation continues by taking A and B from the previous cycle. When $|u_d(k-1) - R_s i_d(k-1)| \geq \lambda$, A and B are updated by means of Equations (12) and (13), and the corresponding compensation calculation is performed. The analysis above shows that the values of A and B are essentially constant over several cycles, so the accuracy of the compensation can be improved.

The control principle block diagram of the proposed RL-MPCC strategy is shown in Figure 4.
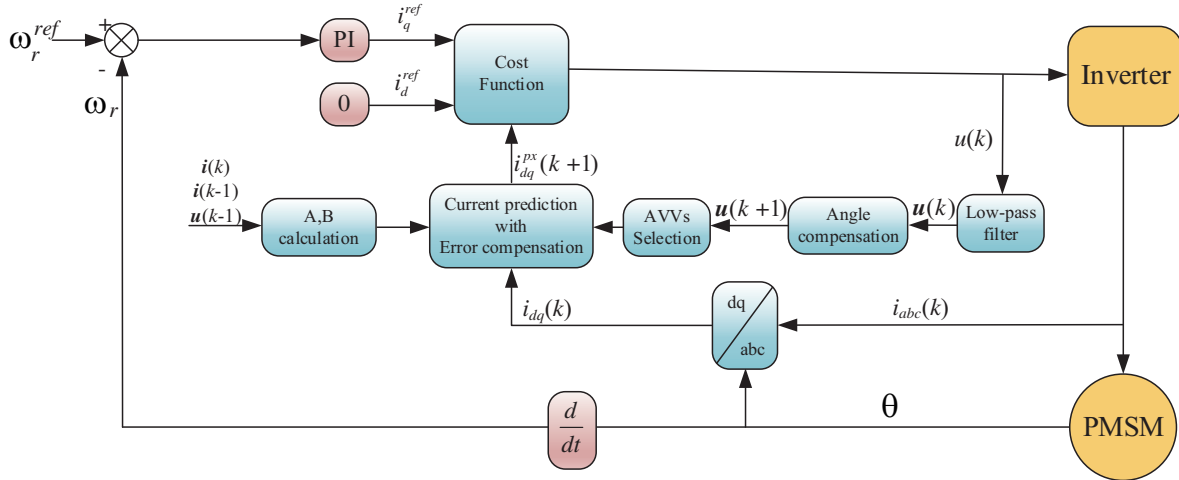

Figure 4. The control principle block diagram of RL-MPCC.

4. EXPERIMENTAL VERIFICATION

Experiments are carried out to verify the correctness and validity of the proposed strategy. The comparison group is RV-MPCC, the proposed RL-MPCC, and RV-MPCC using the correct parameters (CP-MPCC). A Simulink simulation model is built, and the model is downloaded to RT-LAB (OP5600) to realize the hardware in the loop system of PMSM drive system. Figure 5 shows the schematic diagram of RT-LAB hardware in the loop system. The controller adopts TMS320F2812, and the inverter and other parts are constructed by RT-LAB. Figure 6 shows the RT-LAB platform. The PMSM parameters are shown in Table 1. The filter cut-off frequency is set to 1885 rad/s, and the sampling time Ts is 25 μs.

Table 1. Main parameters of PMSM.

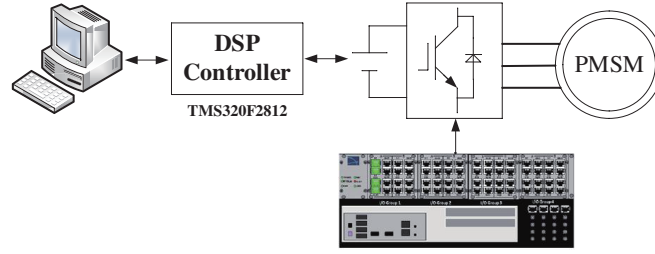| Parameter	Value	Unit
Number of Poles	4	
Permanent magnet flux linkage	0.24	Wb
Stator inductance	8.5	mH
Stator resistance	0.2	Ω
Rated speed	1500	rpm
Rated load	7.15	N·m
Rated voltage	350	V
Rated current	4.9	A
Moment of inertia	0.0012	Kg·m^2

Figure 5. Systemin-the-loop configuration of RT-LAB semi-physical experimental platform.
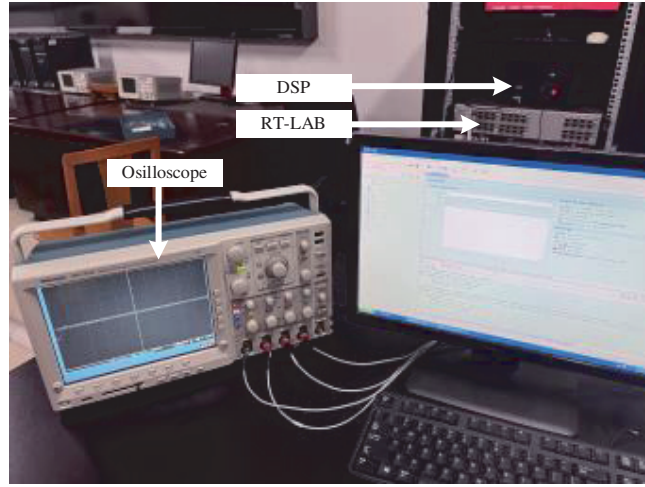

Figure 6. RT-LAB semi-physical experimental platform composition.

4.1. Steady-State Robustness Experiments

To verify the robustness of the proposed RL-MPCC algorithm under inductance and flux linkage parameter mismatch, comparative experiments were conducted with the correct parameters, 50% inductance reduction, and 50% demagnetization, respectively. Parameter mismatch was set by adjusting the motor parameters in the RT-LAB semi-physical simulation platform. RV-MPCC and proposed RL-MPCC use the rated parameters of the motor as prediction parameters. CP-MPCC for the control group is the ideal case, and the prediction parameters follow the motor parameters.

The experimental results of RV-MPCC, RL-MPCC, and CP-MPCC in steady state at 1000 rpm with a load of $7.15\,\mathrm{N\cdot m}$ and without mismatch of motor parameters are shown in Figures 7 and 8. Figure 7 shows from top to bottom the q-axis currents, the reference q-axis currents, and the d-axis currents. Figure 8 shows the A-phase stator current and the Total Harmonic Distortion (THD) of the A-phase stator current. The THD value is obtained by performing Fast Fourier Transform (FFT) analysis of the data acquired by the oscilloscope through MATLAB. The experimental data are shown in Table 2. It can be seen that three strategies have essentially the same performance without parameter

Table 2. Steady-state performance table without parameter mismatch.

Dynamic Response	RV-MPCC	RL-MPCC	CP-MPCC
d axis current fluctuation amplitudes (A)	0.83	0.83	0.83
q axis current fluctuation amplitudes (A)	0.72	0.71	0.71
THD of phase A-phase current	5.05%	5.06%	5.05%

Table 3. Steady-state performance table with 50% inductance reduction.

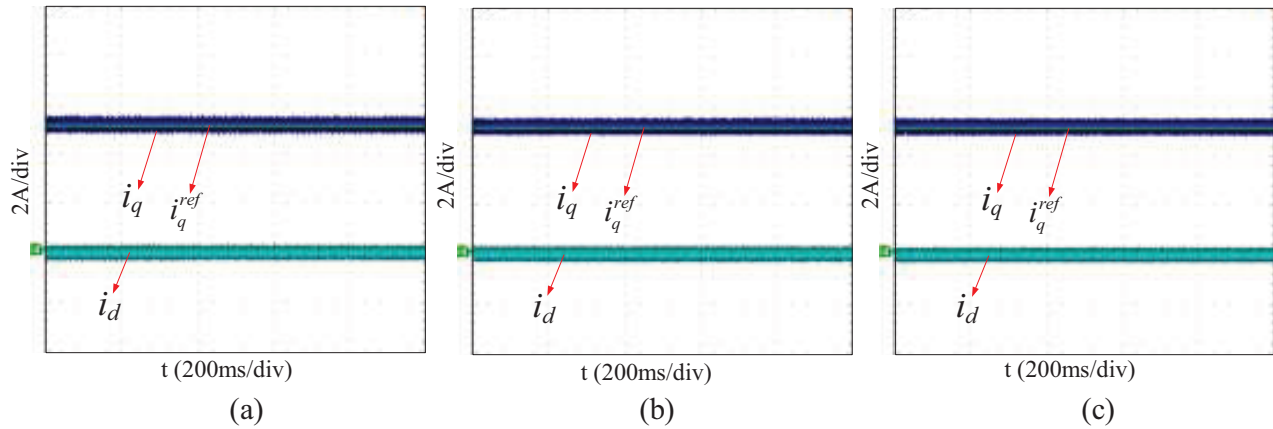| Dynamic Response	RV-MPCC	RL-MPCC	CP-MPCC
d axis current fluctuation amplitudes (A)	2.24	1.52	1.51
q axis current fluctuation amplitudes (A)	1.98	1.26	1.26
THD of phase A-phase current	12.45%	9.71%	9.79%

Figure 7. Experimental results of i_d, i_q, and i_q^{ref} without parameter mismatch. (a) RV -MPCC, (b) RL-MPCC, (c) CP-MPCC.
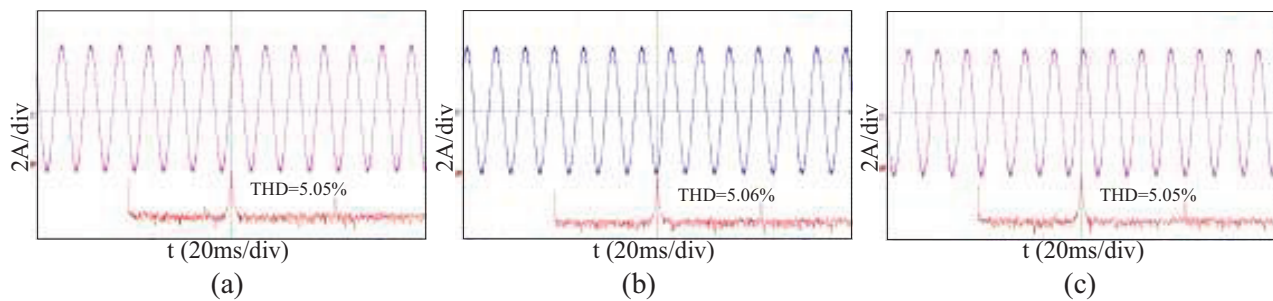

Figure 8. Experimental results of A-phase current and THD without parameter mismatch. (a) RV -MPCC, (b) RL-MPCC, (c) CP-MPCC.

changes, which shows that RL-MPCC has shown good control performance when the parameters are not mismatched.

The experimental results of RV-MPCC, RL-MPCC, and CP-MPCC in steady state at 1000 rpm with a load of $7.15\,\mathrm{N \cdot m}$ and 50% inductance reduction are shown in Figures 9 and 10. The experimental data are shown in Table 3. The current fluctuation amplitudes of the d-q axis of RV-MPCC are 2.24 A and 1.98 A, respectively; those of RL-MPCC are 1.52 A and 1.26 A, respectively; and those of CP-MPCC are 1.51 A and 1.26 A, respectively. The THDs of RV-MPCC, RL-MPCC, and CP-MPCC are 12.45%, 9.71%, and 9.79%, respectively. It can be seen that RV-MPCC strategy is very sensitive to inductance parameter variations, which can cause greater current pulsation and increase the harmonic values, while the RL-MPCC can achieve similar results to the ideal case and compensate well for the prediction errors caused by inductance variations. The proposed strategy RL-MPCC has good robustness to stator inductance parameter deviations.

The experimental results of RV-MPCC, RL-MPCC, and CP-MPCC in steady state at 1000 rpm with a load of $7.15\,\mathrm{N\cdot m}$ and with 50% demagnetization are shown in Figures 11 and 12. The experimental data are shown in Table 4. The current fluctuation amplitudes and THDs of the three strategies are similar, but the q-axis current of the RV-MPCC strategy has a significant deviation compared to the reference value; the RL-MPCC suppresses this offset well; and the control performance is basically the same as that of CP-MPCC. It is verified that the MPCC strategy proposed in this paper still has good immunity to the errors of the permanent flux linkage.

Table 4. Steady-state performance table with 50% demagnetization.

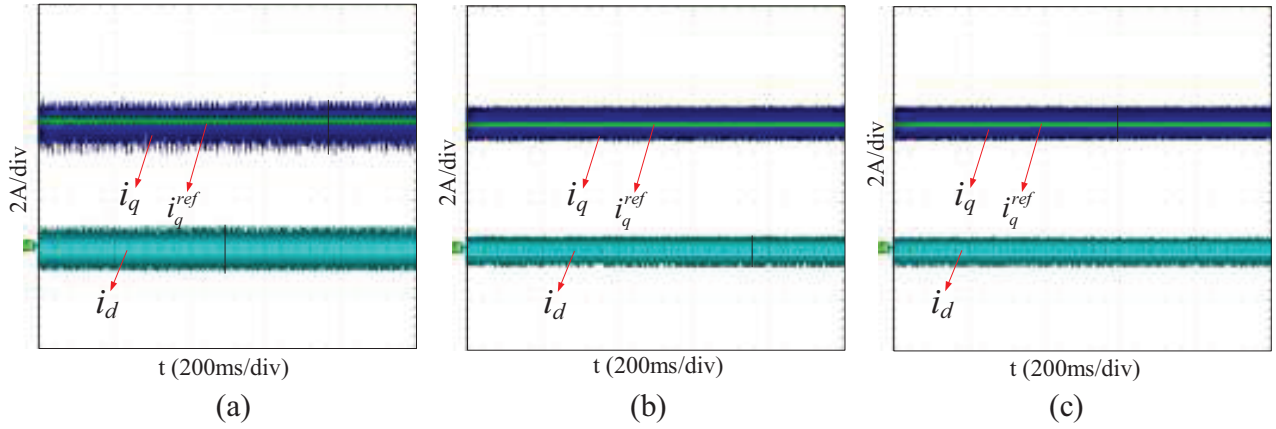| Dynamic Response	RV-MPCC	RL-MPCC	CP-MPCC
d axis current fluctuation amplitudes (A)	0.86	0.86	0.83
q axis current fluctuation amplitudes (A)	0.80	0.83	0.81
THD of phase A-phase current	2.53%	2.54%	2.53%

Figure 9. Experimental results of i_d, i_q, and i_q^{ref} with 50% inductance reduction. (a) RV -MPCC, (b) RL-MPCC, (c) CP-MPCC.
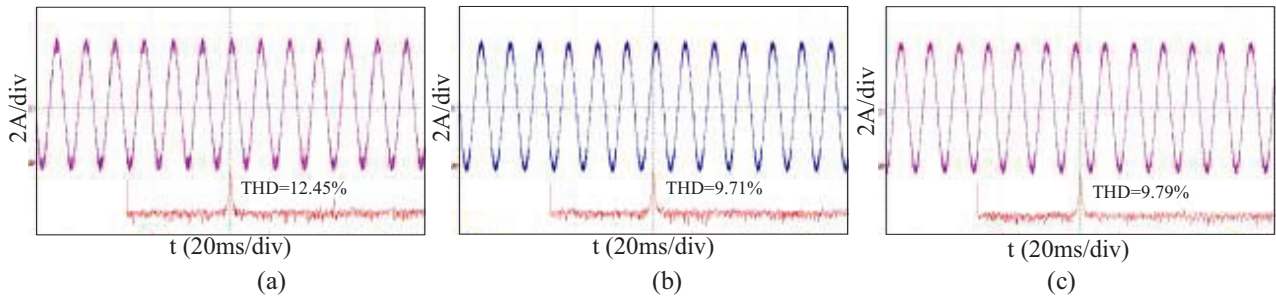

Figure 10. Experimental results of A-phase current and THD with 50% inductance reduction. (a) RV -MPCC, (b) RL-MPCC, (c) CP-MPCC.

4.2. Dynamic Response Experiments

In order to verify the dynamic response of the proposed RL-MPCC, comparative experiments are conducted for the three strategies, including acceleration, deceleration, loading, and unloading. The

first experiment is performed with correct parameters, and the second one is performed with 50% reduction of inductance and flux linkage.

Figure 13 shows the experimental results of the dynamic response of the three strategies without parameter mismatch. After the program is started, the PMSM starts up to the speed of 1000 rpm without load, adds a sudden load of 0.12 N · m at 40 ms, unloads at 80 ms, and finally decelerates to 500 rpm at 120 ms. The experimental data are shown in Table 5. It can be seen that the three strategies have essentially the same response time in the absence of parameter mismatch.

Table 5. Dynamic Response without parameter mismatch Time Table.

Dynamic Response	RV-MPCC	RL-MPCC	CP-MPCC
Start-up time (ms)	8.1	8.09	8.1
Load recovery time (ms)	1.75	1.76	1.75
Unload recovery time (ms)	1.95	1.96	1.95
Speed reduction adjustment time (ms)	7.6	7.6	7.6

(Start-up time: the time for the motor to reach a given speed from zero speed.
Load recovery time: Time to steady state after sudden load.
Unloading recovery time: Time to steady state after sudden unload.
Speed reduction adjustment time: the time for the motor to reach a given speed from a higher given speed.)
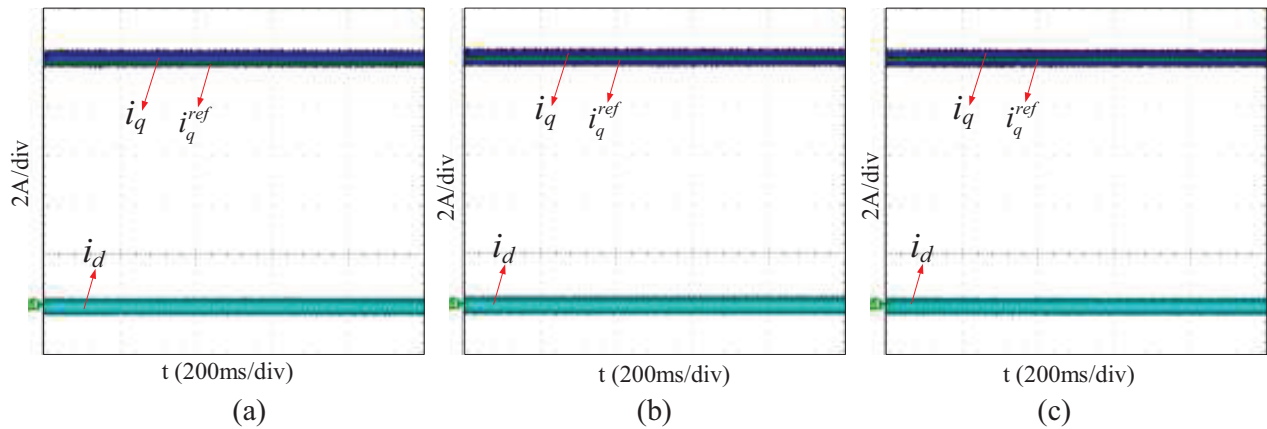

(a)　　　　　　(b)　　　　　　(c)

Figure 11. Experimental results of i_d, i_q, and i_q^{ref} with 50% demagnetization. (a) RV -MPCC, (b) RL-MPCC, (c) CP-MPCC.
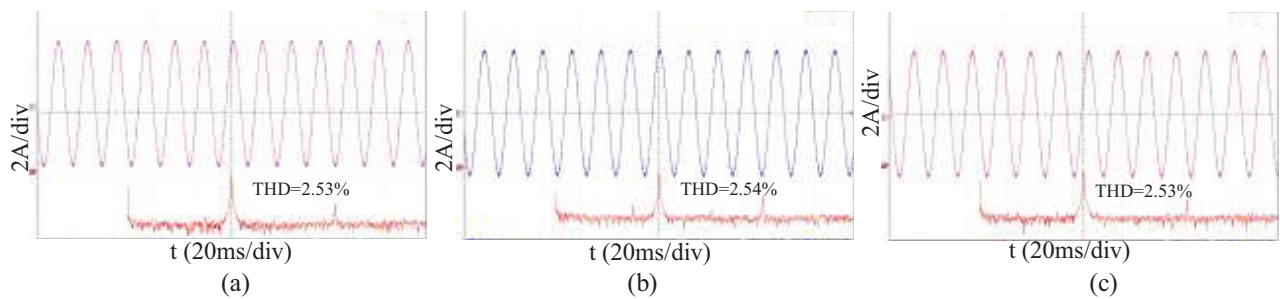

(a)　　　　　　(b)　　　　　　(c)

Figure 12. Experimental results of A-phase current and THD with 50% demagnetization. (a) RV -MPCC, (b) RL-MPCC, (c) CP-MPCC.
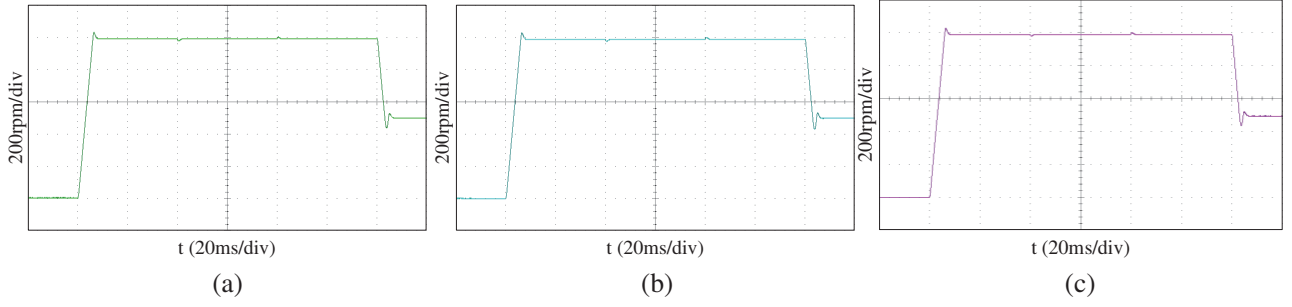
Figure 13. Dynamic response experimental results without parameter mismatch. (a) RV-MPCC, (b) RL-MPCC, (c) CP-MPCC.
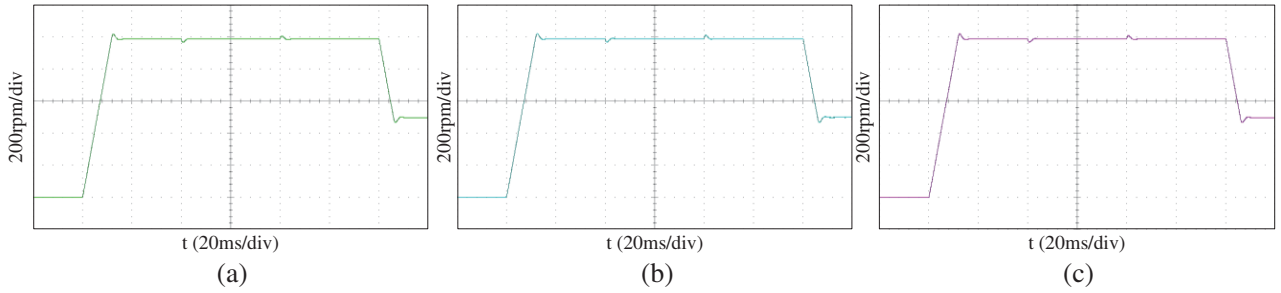

Figure 14. Dynamic response experimental results with 50% reduction of inductance and flux linkage. (a) RV-MPCC, (b) RL-MPCC, (c) CP-MPCC.

Figure 14 shows the experimental results of the dynamic response of the three strategies with 50% reduction of inductance and flux linkage. After the program is started, the PMSM starts up to the speed of 1000 rpm without load, adds a sudden load of $0.12 \, \text{N} \cdot \text{m}$ at 40 ms, unloads at 80 ms, and finally decelerates to 500 rpm at 120 ms. The experimental data are shown in Table 6. From the comparison of Table 5 and Table 6, it can be seen that the inductance and magnetic chain reduction leads to a slower dynamic response of the motor, and all kinds of response times increase significantly. The response time of RV-MPCC is slightly increased compared to that of CP-MPCC under the same operating conditions, which is consistent with the analysis in [14] that parameter mismatch has little effect on the dynamic response of the motor. The response time of RL-MPCC is similar to that of CP-MPCC, and even shorter than CP-MPCC in terms of acceleration time and unloading time.

Table 6. Dynamic Response with 50% reduction of inductance and flux linkage.

Dynamic Response	RV-MPCC	RL-MPCC	CP-MPCC
Start-up time (ms)	16.4	16.3	16.4
Load recovery time (ms)	4.5	4.3	4.3
Unload recovery time (ms)	4.6	4.5	4.55
Speed reduction adjustment time (ms)	10.5	10.5	10.4

Overall, it is experimentally demonstrated that the proposed RL-MPCC strategy ensures superior dynamic response characteristics of the model predictive control while improving the robustness to inductor and permanent magnet chain mismatch.

5. CONCLUSION

To solve the problems of excessive computational burden and degradation of prediction performance due to parameter mismatch, a robust, low-complexity MPCC strategy for PMSM is proposed in this paper. The following conclusions are drawn through simulation and experimental analysis:

1) A low-pass filter and angle compensation are introduced to obtain the actual voltage. AVVs are selected according to the location of the actual voltage vector, and the number of AVVs is decreased so reducing the computational burden. It can be verified by simulation that the proposed strategy can reduce the number of AVVs at steady state. The average number of AVVs per cycle is only 4.1 when the motor is operated at 1500 rpm.

2) A prediction error compensation method is designed to compensate the prediction current error due to inductance and flux linkage variations. The comparison of the three strategies shows that the proposed strategy has robustness to the mismatch of motor inductance and flux linkage and can obtain steady state performance similar to that of the ideal case of CP-MPCC. At the same time, the proposed MPCC strategy also maintains a superior dynamic response.

REFERENCES

1. Kefalas, T. D. and A. G. Kladas, "Thermal investigation of Permanent-Magnet synchronous motor for aerospace applications," *IEEE Transactions on Industrial Electronics*, Vol. 61, No. 8, 4404–4411, Aug. 2014, doi: 10.1109/TIE.2013.2278521.

2. Chen, L., H. Xu, X. Sun, and Y. Cai, "Three-vector-based model predictive torque control for a permanent magnet synchronous motor of EVs," *IEEE Transactions on Transportation Electrification*, Vol. 7, No. 3, 1454–1465, Sept. 2021, doi: 10.1109/TTE.2021.3053256.

3. Li, S., Y. Xu, W. Zhang, and J. Zou, "A novel two-phase mode switching control strategy for PMSM position servo systems with fast-response and high-precision," *IEEE Transactions on Power Electronics*, Vol. 38, No. 1, 803–815, Jan. 2023, doi: 10.1109/TPEL.2022.3200969.

4. Repecho, V., J. B. Waqar, D. Biel and A. Dòria-Cerezo, "Zero speed sensorless scheme for permanent magnet synchronous machine under decoupled sliding-mode control," *IEEE Transactions on Industrial Electronics*, Vol. 69, No. 2, 1288–1297, Feb. 2022, doi: 10.1109/TIE.2021.3062260.

5. Yi, P., X. Wang, D. Chen, and Z. Sun, "PMSM current harmonics control technique based on speed adaptive robust control," *IEEE Transactions on Transportation Electrification*, Vol. 8, No. 2, 1794–1806, Jun. 2022, doi: 10.1109/TTE.2021.3128535.

6. Gu, M., et al., "Finite control set model predictive torque control with reduced computation burden for PMSM based on discrete space vector modulation," *IEEE Transactions on Energy Conversion*, Vol. 38, No. 1, 703–712, Mar. 2023, doi: 10.1109/TEC.2022.3211569.

7. Chen, W., S. Zeng, G. Zhang, T. Shi, and C. Xia, "A modified double vectors model predictive torque control of permanent magnet synchronous motor," *IEEE Transactions on Power Electronics*, Vol. 34, No. 11, 11419–11428, Nov. 2019, doi: 10.1109/TPEL.2019.2898901.

8. Petkar, S. G., K. Eshwar, and V. K. Thippiripati, "A modified model predictive current control of permanent magnet synchronous motor drive," *IEEE Transactions on Industrial Electronics*, Vol. 68, No. 2, 1025–1034, Feb. 2021, doi: 10.1109/TIE.2020.2970671.

9. Wu, M., X. Sun, J. Zhu, G. Lei, and Y. Guo, "Improved model predictive torque control for pmsm drives based on duty cycle optimization," *IEEE Transactions on Magnetics*, Vol. 57, No. 2, 1–5, Feb. 2021, Art No. 8200505, doi: 10.1109/TMAG.2020.3008495.

10. Mamdouh, M. and M. A. Abido, "Efficient predictive torque control for induction motor drive," *IEEE Transactions on Industrial Electronics*, Vol. 66, No. 9, 6757–6767, Sept. 2019, doi: 10.1109/TIE.2018.2879283.

11. Amiri, M., J. Milimonfared, and D. A. Khaburi, "Predictive torque control implementation for induction motors based on discrete space vector modulation," *IEEE Transactions on Industrial Electronics*, Vol. 65, No. 9, 6881–6889, Sept. 2018, doi: 10.1109/TIE.2018.2795589.

12. Xie, H., F. Wang, Q. Xun, Y. He, J. Rodríguez, and R. Kennel, "A low-complexity gradient descent solution with backtracking iteration approach for finite control set predictive current control," *IEEE Transactions on Industrial Electronics*, Vol. 69, No. 5, 4522–4533, May 2022, doi: 10.1109/TIE.2021.3084164.

13. Wang, Y., et al., "Deadbeat model-predictive torque control with discrete space-vector modulation for PMSM drives," *IEEE Transactions on Industrial Electronics*, Vol. 64, No. 5, 3537–3547, May 2017, doi: 10.1109/TIE.2017.2652338.

14. Sun, X., T. Li, Z. Zhu, G. Lei, Y. Guo, and J. Zhu, "Speed sensorless model predictive current control based on finite position set for PMSHM drives," *IEEE Transactions on Transportation Electrification*, Vol. 7, No. 4, 2743–2752, Dec. 2021, doi: 10.1109/TTE.2021.3081436.

15. Sun, X., T. Li, M. Yao, G. Lei, Y. Guo, and J. Zhu, "Improved finite-control-set model predictive control with virtual vectors for PMSHM drives," *IEEE Transactions on Energy Conversion*, Vol. 37, No. 3, 1885–1894, Sept. 2022, doi: 10.1109/TEC.2021.3138905.

16. Young, H. A., M. A. Perez, and J. Rodriguez, "Analysis of finite-control-set model predictive current control with model parameter mismatch in a three-phase inverter," *IEEE Transactions on Industrial Electronics*, Vol. 63, No. 5, 3100–3107, May 2016, doi: 10.1109/TIE.2016.2515072.

17. Li, T., X. Sun, G. Lei, Y. Guo, Z. Yang, and J. Zhu, "Finite-control-set model predictive control of permanent magnet synchronous motor drive systems — An overview," *IEEE/CAA Journal of Automatica Sinica*, Vol. 9, No. 12, 2087–2105, Dec. 2022, doi: 10.1109/JAS.2022.105851.

18. Liu, S. and C. Liu, "Virtual-vector-based robust predictive current control for dual three-phase PMSM," *IEEE Transactions on Industrial Electronics*, Vol. 68, No. 3, 2048–2058, Mar. 2021, doi: 10.1109/TIE.2020.2973905.

19. Mousavi, M. S., et al., "Predictive torque control of induction motor based on a robust integral sliding mode observer," *IEEE Transactions on Industrial Electronics*, Vol. 70, No. 3, 2339–2350, Mar. 2023, doi: 10.1109/TIE.2022.3169831.

20. An, X., G. Liu, Q. Chen, W. Zhao, and X. Song, "Adjustable model predictive control for IPMSM drives based on online stator inductance identification," *IEEE Transactions on Industrial Electronics*, Vol. 69, No. 4, 3368–3381, Apr. 2022, doi: 10.1109/TIE.2021.3076718.

21. Huang, X., Y. Yu, Z. Li, et al., "Online identification of inductance and flux linkage for inverter-fed SPMSMs using switching state functions," *IEEE Transactions on Power Electronics*, Vol. 38, No. 1, 917–930, Jan. 2023, doi: 10.1109/TPEL.2022.3206119.

22. Wang, Y., W. Liao, S. Huang, et al., "A robust DPCC for IPMSM based on a full parameter identification method," *IEEE Transactions on Industrial Electronics*, Vol. 70, No. 8, 7695–7705, Aug. 2023, doi: 10.1109/TIE.2022.3212371.

23. Sun, Z., Y. Deng, J. Wang, T. Yang, Z. Wei, and H. Cao, "Finite control set model-free predictive current control of PMSM with two voltage vectors based on ultralocal model," *IEEE Transactions on Power Electronics*, Vol. 38, No. 1, 776–788, Jan. 2023, doi: 10.1109/TPEL.2022.3198990.

24. Zhou, Y., H. Li, R. Liu, and J. Mao, "Continuous voltage vector model-free predictive current control of surface mounted permanent magnet synchronous motor," *IEEE Transactions on Energy Conversion*, Vol. 34, No. 2, 899–908, Jun. 2019, doi: 10.1109/TEC.2018.2867218.

25. Siami, M., D. A. Khaburi, A. Abbaszadeh, and J. Rodríguez, "Robustness improvement of predictive current control using prediction error correction for permanent-magnet synchronous machines," *IEEE Transactions on Industrial Electronics*, Vol. 63, No. 6, 3458–3466, Jun. 2016, doi: 10.1109/TIE.2016.2521734.

26. Zhang, X., L. Zhang, and Y. Zhang, "Model predictive current control for PMSM drives with parameter robustness improvement," *IEEE Transactions on Power Electronics*, Vol. 34, No. 2, 1645–1657, Feb. 2019, doi: 10.1109/TPEL.2018.2835835.